

## Are mesoscale eddies in shelf seas formed by baroclinic instability of tidal fronts?

G. Badin,<sup>1</sup> R. G. Williams,<sup>1</sup> J. T. Holt,<sup>2</sup> and L. J. Fernand<sup>3</sup>

Received 23 February 2009; revised 15 July 2009; accepted 23 July 2009; published 27 October 2009.

[1] The formation of eddies along tidal fronts in the shelf seas is investigated through both the analysis of high-resolution conductivity-temperature-depth (CTD) data and drifters for the North Sea as well as experiments with an eddy-permitting model. Baroclinic eddies are difficult to observe in the shelf seas due to their small size, and their surface signals are damped by air-sea interaction and eroded by wind and tidal mixing. High-resolution CTD profiles reveal possible eddy signals along the thermocline where there are intrusions of waters of reduced salinity on the eddy scale. These freshwater intrusions carry low potential vorticity, indicating their origin from the surface mixed layer. An instability analysis of these frontal systems suggests that these eddy signals can be formed by baroclinic instability. Numerical model integrations reveal that mesoscale eddy variability along the thermocline increases in strength in late summer, in accord with the increase in stratification. The stability analysis of the modeled fronts and the scaling of the eddy kinetic energy to the available potential energy are also consistent with baroclinic instability theory. While influencing the eddy variability through the passage of synoptic weather systems, wind energy input is too small to explain the high values of eddy kinetic energy during late summer. These eddy circulations provide localized regions of high vorticity and high stirring, which are important for the transfer of tracers at middepth, such as potential vorticity, salinity, and nutrients.

**Citation:** Badin, G., R. G. Williams, J. T. Holt, and L. J. Fernand (2009), Are mesoscale eddies in shelf seas formed by baroclinic instability of tidal fronts?, *J. Geophys. Res.*, *114*, C10021, doi:10.1029/2009JC005340.

### 1. Introduction

[2] Despite the leading role that baroclinic eddies have in the atmosphere and their importance in the open ocean, the formation of eddies in shelf seas remains unclear: are mesoscale eddies created by baroclinic instabilities? What are their typical signals and length and time scales? How does seasonality affect their formation process?

[3] Our hypothesis is that eddies are formed along tidal fronts in shelf seas due to baroclinic instability of the front, rather than through wind-induced formation. In this case study, an ensemble of observations and modeling over the same period are interpreted to assess likely eddy signals and the role of baroclinic instability in the southern North Sea. In section 2, possible eddy signals are examined using Scanfish data through the summer thermocline and in drifters data. The stability criteria are studied both for a high-resolution Scanfish section and an eddy-resolving numerical model. The typical horizontal scale and formation time of baroclinic instabilities in the shelf seas is examined. In section 3, the eddy-resolving numerical model is used to examine how the

energetics of the eddies vary seasonally; to study the relationships between the eddy kinetic energy, the available potential energy and the wind energy input; and to test if the energetics are consistent with baroclinic instability theory. In section 4, the model is used to study where persistent mesoscale signals are and their effects on the cross-front transfer.

### 2. Observations of Possible Eddy Signatures

[4] There is a range of different fronts in shelf seas: upwelling fronts [e.g., Barth, 1989b], haline fronts [e.g., Sharples and Simpson, 1993] and tidal mixing fronts [e.g., Simpson and Hunter, 1974]. Tidal mixing fronts separate well mixed and stratified waters and have typical horizontal cross-front length of  $O(\leq 10 \text{ km})$  and along-front length of  $O(\geq 100 \text{ km})$ . For comparison, open ocean fronts divide two regions of stratified waters and can have along-front length of  $O(\geq 1000 \text{ km})$ .

[5] Baroclinic eddies have been observed in the shelf seas, such as in the Celtic Sea [Pingree, 1978, 1979], on the Oregon Shelf [Barth *et al.*, 2005], in the California Current System [Castelao *et al.*, 2006], in the Black Sea [Zatsepina *et al.*, 2003] and in the Yellow Sea [Yanagi *et al.*, 1996]. In this study we make the hypothesis that mesoscale eddies are formed along tidal fronts due to baroclinic instability of the front, in accord with modeling studies, such as Simpson and James [1986] and Thiem *et al.* [2006].

[6] Identifying shelf sea eddies along tidal fronts in the Northwest European Shelf in satellite images is difficult

<sup>1</sup>Department of Earth and Ocean Sciences, University of Liverpool, Liverpool, UK.

<sup>2</sup>Proudman Oceanographic Laboratories, Liverpool, UK.

<sup>3</sup>Centre for Environment, Fisheries and Aquaculture Science, Lowestoft, UK.

though due to the small size of the eddies and to the damping of sea surface temperature signals from air-sea interaction and from enhanced mixing at the tidal front. Given this difficulty of detecting surface signals of eddies, we consider high-resolution Scanfish section and drifter data within the summer thermocline for the southern North Sea.

## 2.1. Frontal Circulation in the North Sea

[7] In this section, towed undulating conductivity-temperature-depth (Scanfish) data are examined off the Dogger Bank in the North Sea (Figure 1a) during the period between 15 and 31 August 2001 (Cruise R/V Corystes, Centre for Environment, Fisheries and Aquaculture Science; CEFAS) to study stratification and water mass signals linked with possible mesoscale eddies. Data have a typical horizontal resolution of 4 m and typical vertical resolution of 0.5 m. Over the deeper waters, the Scanfish data reveal a surface mixed layer in the upper 10 m, then a double thermocline with higher stratification from 15 m to 45 m, and weak stratification below 50 m (Figure 1b). Conversely, over the Dogger Bank, there is a grounding of the lower thermocline and weak stratification.

[8] In the southern North Sea, the horizontal circulation consists of a baroclinic jet along the side of the Dogger Bank [Brown et al., 1999, 2001] accompanying the stratification gradients (Figure 1b). The baroclinic jet is responsible for the advection of riverine freshwaters from the coast to the basin interior, as revealed by large salinity minima, <34.6 psu (Figure 1c). In addition, there are bottom fronts separating the well-mixed region over the Dogger Bank and the stratified region to the north (Figure 1b).

[9] Along the thermocline, there are horizontal undulations in the density structure away from the Dogger Bank, which are associated with water mass changes. There are low salinity anomalies at the position  $\approx 20\text{--}25$  km (Figure 1c) along the lower thermocline, defined by  $\sigma = 26.5$  to 27.1, where the analysis is made with data binned horizontally with resolution of 1 km and vertically with resolution of 1 m. The low salinity anomalies have salinity values comparable to the baroclinic jet along the Dogger Bank (Figure 1e, continuous line).

## 2.2. How Are the Localized Salinity Minima Formed?

[10] Low salinity values are not present in the density layers above or below the lower thermocline (Figure 1c), so that this freshwater signal cannot be transferred there through vertical mixing from wind or tidal forcing. If the intrusions originated from smaller baroclinic jets, they would be present with a similar structure in other parallel sections, but this signal is not seen in other sections (not shown) parallel to the baroclinic jet. The intrusions might also possibly originate from the spring-neap cycle through turbulent entrainment, but again there should be a signal of the intrusions at constant separation from each other in all the sections.

[11] Alternatively, the low salinity anomaly might be consequence of the eddy transfer from the jet. In order to test this hypothesis, the salinity and the large-scale potential vorticity,

$$PV = -\frac{f}{\rho_0} \frac{\partial \sigma}{\partial z}, \quad (1)$$

distributions are compared along the lower thermocline (Figure 1d). Along the lower thermocline the potential vorticity distribution (Figure 1e, dashed line) reveals two minima, corresponding to the salinity minima in the well-mixed region and in the thermocline intrusion. The coincidence of low potential vorticity and salinity, together with the quasi-conservation of potential vorticity in the thermocline, where mixing is weak, allows one to track the origin of these intrusions from the well-mixed region of the baroclinic jet to the lower thermocline in the deeper waters.

[12] In our view, the freshwater thermocline intrusions are probably associated with baroclinic eddies, with horizontal scale of 5 km. The thermocline intrusions are also associated with enhanced fluorescence (Figure 1f), suggesting that eddy transfer of nutrients along the thermocline is enhancing biological production there.

[13] In the shelf seas, thermocline eddies have been observed for example in the southern North Sea [van Aken et al., 1987] and in the Baltic Sea [Zhurbas et al., 2004]. Intrathermocline eddies have been observed also in the open ocean (see the reviews by McWilliams [1985] and Kostianoy and Belkin [1989]), in the Atlantic Ocean (“Meddies” [Armi and Zenk, 1984]), in the Indian Ocean (“Reddies” [Shapiro and Meschanov, 1991]) and in the Arctic Ocean [D’Asaro, 1988]. The intrusions formed at fronts are usually observed to carry low potential vorticity signals [Thomas, 2008]. In the open ocean, the low potential vorticity of intrusions are formed at frontal regions and subducted into the thermocline. In shelf seas, the low potential vorticity signal is probably created by the lateral transfer of low stratification from boundary regions of tidal and wind mixing.

## 2.3. Possible Eddy Signals in Drifter Data

[14] To assess whether there is a more robust eddy signal, drifter data are analyzed (Figure 2). Data come from 23 Argos Satellite tracked drifting buoys deployed in the summer of 2001 by CEFAS and The Irish Marine Institute (R/V Corystes: cruise 6 and R/V Celtic Voyager: cruise 34) for periods ranging from 8 to 62 days. The drifters have a 5.5 m drogue centered at 30 m depth. To estimate subtidal velocities, the drifter positions are linearly interpolated to give an hourly time series, which is filtered to remove energy at semidiurnal and diurnal tidal frequencies [Holt and Proctor, 2008].

[15] While the main motion of the drifters is eastward following density-driven flow [Brown et al., 1999], they show considerable variation in their paths, particularly as they pass north of Dogger Bank along the 40 m isobath (Figure 2a). This motion is clearly a combination of mean flow and a rotational motion. For example, Figure 2b shows the track of drifter 59395, the same track low-pass filtered by a 6 day running mean, and the residual high-frequency circulation. The high-frequency component reveals the rotational motion of the eddies. By applying this technique to each of the tracks, the characteristic radius for the rotational motion is found to be  $L = 3.2$  km and a mean rotational speed of  $U = 0.017 \text{ m s}^{-1}$ . These rotational values correspond to a characteristic frequency of  $\omega = 2 \pi \langle U_i/L_i \rangle = 1.33 \times 10^{-5} \text{ s}^{-1}$ , where  $\langle U_i/L_i \rangle$  indicates that the frequency is calculated from the average of the ratios of the characteristic velocities and radii of the rotational motion for each

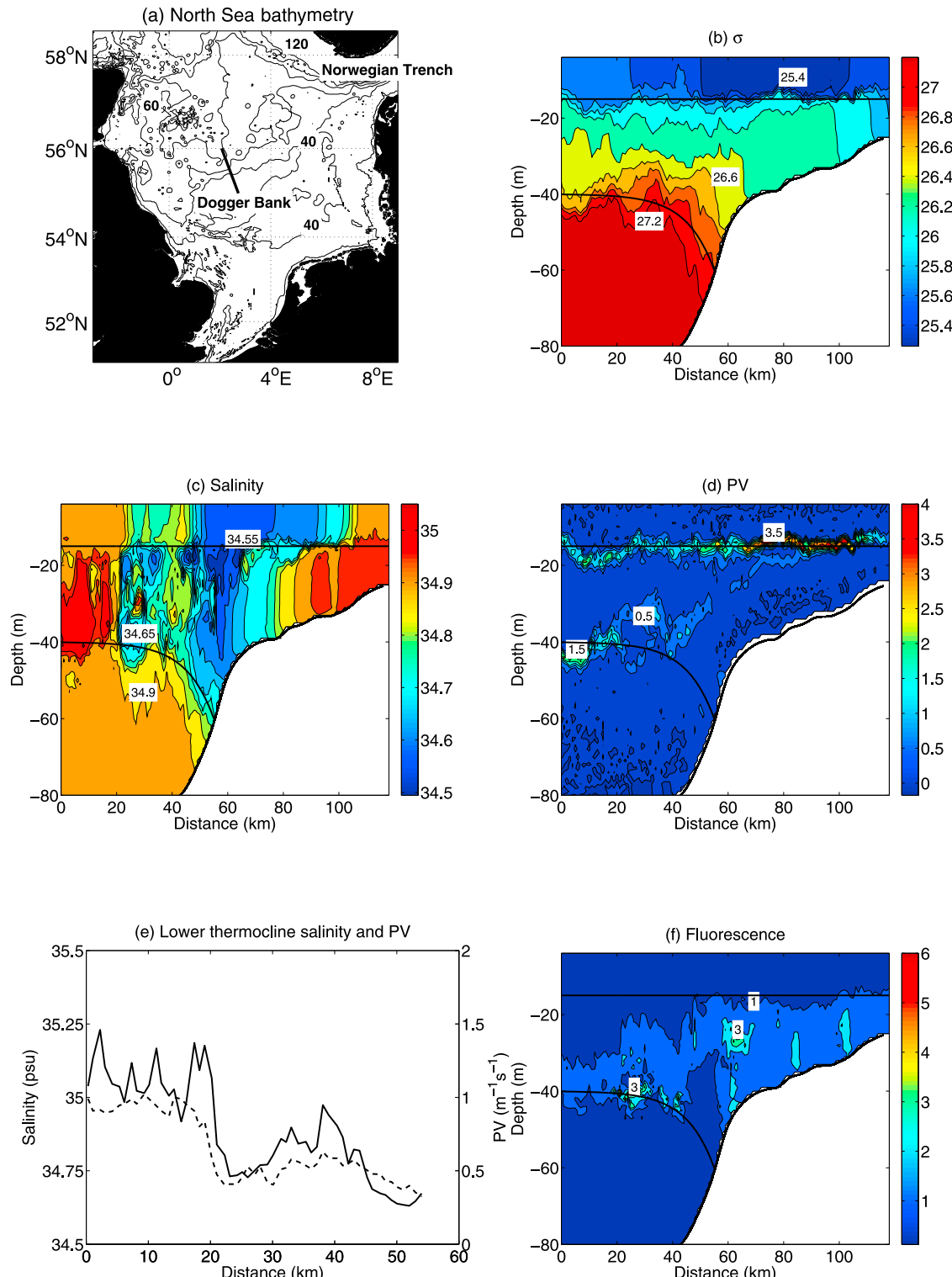


**Figure 1.** (a) North Sea bathymetry. Isobaths are shown every 20 m. (b) Vertical sections of  $\sigma$  density; (c) salinity (psu); (d) potential vorticity ( $10^{-8} \text{ m}^{-1} \text{ s}^{-1}$ ); (e) lower thermocline salinity (dashed line) and potential vorticity (continuous line); and (f) fluorescence from a high-resolution Scanfish section on 16 August 2001, north of the Dogger Bank (thick black line in Figure 1a). South is to the right. Note the freshwater intrusions at 25 km, which are on the eddy scale. The thick lines represent the interfaces of the three-layer approximation.

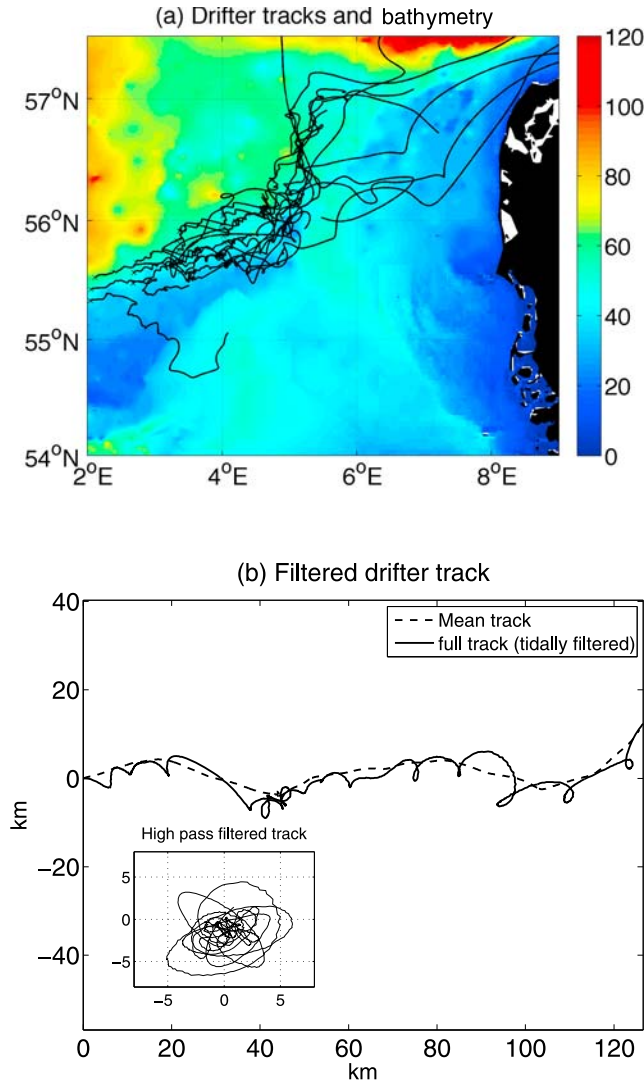


**Figure 2.** (a) Tracks from 23 Argo satellite tracked drifting buoys deployed in the summer of 2001 together with the bathymetry (m). (b) Drifter track from one of the drifters in Figure 2a (scale in km). The track has been low-pass filtered, and this has been subtracted to show the rotational eddy motion relative to the background displacement (inset).

drifter, and thus  $\omega/f < 1$ , which excludes the hypothesis that the observed rotational motion are due to inertial oscillations. The rotational motion is primarily anticyclonic, in accord with laboratory [Griffiths and Hopfinger, 1984; Linden et al., 1995] and idealized modeling studies [Stegner and Dritschel, 2000] revealing that anticyclonic baroclinic eddies are more common, coherent and energetic in shallow water turbulence.

[16] A source of error in the previous estimates might arise from the fact that the drifters might not sample the core of the eddies but that they remain constrained in the strain dominated regions between the eddies, where the dynamics take the form of chaotic advection [Waugh et al., 2006].

[17] Given the existence of possible signals of eddies in the observational data, in section 2.4 we analyze the stability of the fronts present in the high-resolution Scanfish section.

## 2.4. Stability Analysis

[18] In the open ocean, baroclinic eddies are primarily formed by the baroclinic instability process, acting to extract available potential energy from the tilting of isopycnals, which is converted to eddy kinetic and potential energy. Available potential energy is, for example, provided by wind forcing over the basin scale in weak midlatitude gyres [Gill et al., 1974] or along the Antarctic Circumpolar Current [e.g., Bryden, 1979]. Baroclinic eddies are then produced, for example, through the instability of western boundary currents; in the interior [Spall, 2000]; or in presence of weak potential vorticity gradients throughout much of the water column, which satisfies the necessary condition for baroclinic instability that meridional potential vorticity gradients must vanish somewhere in the water column [Charney and Stern, 1962].

[19] In the shelf seas, the available potential energy is provided by the combination of buoyancy forcing and tidal and wind mixing, which act to maintain the gradient of baroclinicity. Seasonal development of baroclinicity is thus affected by the seasonal buoyancy forcing, as well as by the changes in mechanical forcing.

[20] In shelf seas, baroclinic instability is modified by shallow water dynamics, finite depths and bottom friction. The instability of shelf sea fronts has been studied in detail by Killworth et al. [1984], who found that, for finite depth shallow water dynamics, the equilibrium is always unstable regardless of the distribution of potential vorticity.

[21] The stability of tidal fronts is also influenced by the strong bottom slopes of bathymetry in proximity of the fronts. Orlansky [1969] analyzed the stability of a two-layer model using the shallow water approximation, finding the stabilizing effect of a bottom topography sloping in the same sense of the slope of the interface. The same result was found by Barth [1989b], who applied the stability analysis to a two-layer shallow water model with a surface upwelling front. It might be noted that for bottom tidal fronts, the interface between the layers slopes in the opposite sense of the bottom topography, avoiding thus the stabilizing effect. The stability of tidal fronts is also influenced by bottom friction. Barth [1989b] found that friction introduces a phase shift in the disturbance, allowing the wave to release energy from the basic state flow, with an energy gain larger than the loss of energy to the dissipation, and thus allowing the disturbances to grow.

### 2.4.1. Stability Criteria

[22] The quasi-geostrophic necessary conditions for stability criteria for layered model [Charney and Stern, 1962; Pedlosky, 1964] are

$$\overline{u}_i \frac{\partial Q_i}{\partial y} \geq 0 \quad (2)$$

$$\frac{\partial Q_i}{\partial y} \leq 0 \quad (3)$$

where  $\overline{u}_i$ ,  $i = 1, 2$ , is the zonal mean flow in the upper and middle layers,  $Q_i = \frac{f}{h_i} \frac{\partial \overline{u}_i}{\partial y}$ ,  $i = 1, 2$  is the mean potential vorticity in the upper and middle layer and  $Q_3 = \frac{f}{h_3}$  is the mean potential vorticity in the lower layer, where  $\overline{u}_3 = 0$ , and  $h_i$ ,  $i = 1, 2, 3$  are the layer thicknesses.

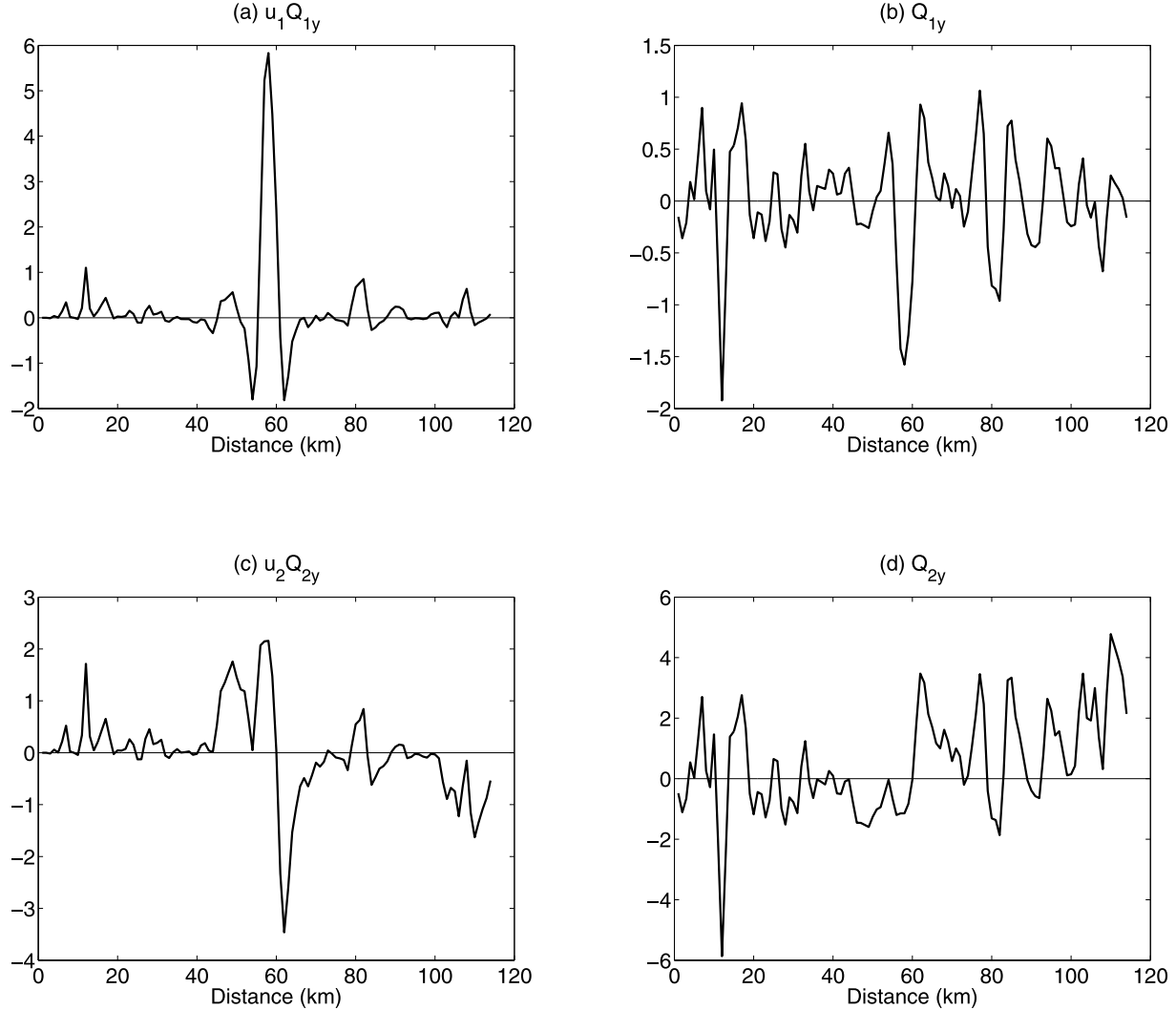


**Figure 3.** Stability criteria analysis for the (a and b) top and (c and d) middle layers for the high-resolution Scanfish section north of the Dogger Bank for the three-layer approximation. South is to the right.

[23] In shelf seas tidal fronts, due to the steep slope of isopycnals and bottom topography, the quasi-geostrophic approximation does not generally hold. Necessary conditions for stability criteria can be found using the conservation of energy and momentum: if  $E_w$  and  $M_w$  are the conserved energy and momentum, respectively, of the wave-wave interactions in the semigeostrophic approximation [Hoskins, 1975], and if  $\gamma$  is a coupling constant with dimensions  $m s^{-1}$ , the conservation of the quantity  $E_w - \gamma M_w$  leads to the stability criteria [Barth, 1989a]

$$(\bar{u}_i - \gamma) \frac{\partial Q_i}{\partial y} \geq 0 \quad (4)$$

$$\gamma \frac{\partial Q_i}{\partial y} \leq 0 \quad (5)$$

$$\frac{\bar{h}_{i+1}}{\bar{h}_i} (\bar{u}_i - \gamma)^2 + \gamma^2 \leq g'_{i+1} \bar{h}_{i+1} \quad (6)$$

where, for (6) and (4),  $i = 1, 2$ , while for (5),  $i = 1, 2, 3$ . If any of (4) and (5) are not satisfied, the system might be unstable. As noted by Barth [1989a], (4) and (5) correspond to (2) and (3), even if for the derivation of (4) and (5) make no use of the quasi-geostrophic approximation. The necessary condition for stability (6) requires the existence of a mean flow that is everywhere less than the internal gravity wave phase speed  $(g'_{i+1} \bar{h}_{i+1})^{1/2}$ . Due to the weakness of the flows considered here, this condition is readily satisfied. In the following analysis, (4) and (5) will be examined to assess the instability of the shelf sea fronts.

#### 2.4.2. Stability Analysis of the Observed Fronts

[24] To assess the stability of the frontal system north of the Dogger Bank, the system is approximated to a three-layer model. The interface separating the top to the middle layer is approximated to be flat at a constant depth of  $\bar{h}_1 = -15$  m, corresponding to the upper thermocline. The interface separating the middle to the bottom layer is approximated to an exponential profile  $\bar{h}_2 = H_3 + a \exp[b(y + c)]$ , where  $H_3 = -40$  m,  $a = -20$  m,  $b = 0.1 \text{ km}^{-1}$  and  $c = -56$  km (Figure 1, thick black lines). The analysis of the necessary conditions for stability (4) and (5) reveal changes of sign of both  $\bar{u}_i \frac{\partial Q_i}{\partial y}$

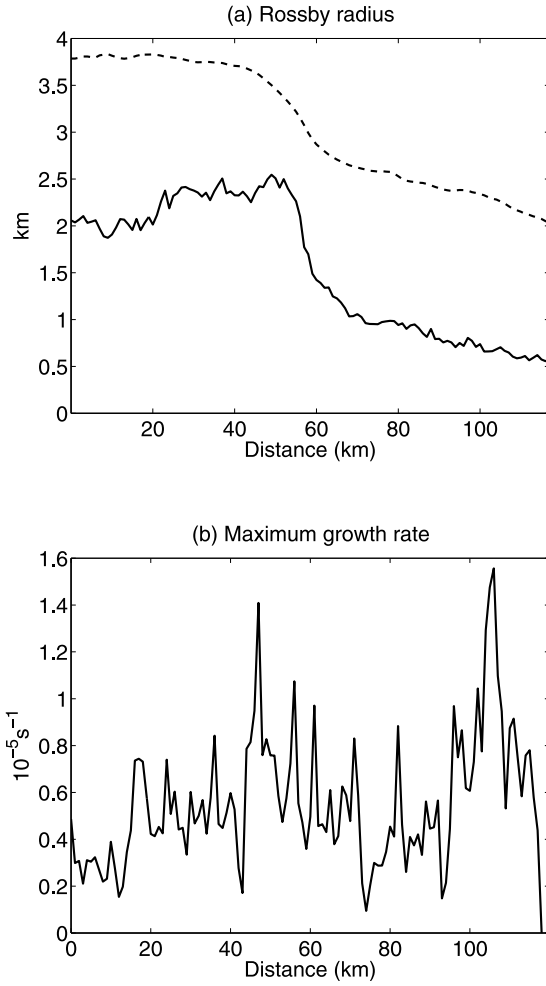


**Figure 4.** Eddy scales diagnosed from the high-resolution Scanfish section north of the Dogger Bank: (a) First baroclinic (continuous line) and two-layer (dashed line) Rossby radii of deformation (km). (b) Maximum Eady growth rate ( $s^{-1}$ ). South is to the right.

and  $\frac{\partial Q}{\partial y}$  along the whole domain (Figure 3). The necessary conditions for stability are thus not satisfied and the system might be baroclinically unstable. Note that the analysis of the necessary condition for stability, (4) (Figures 3a and 3c), shows larger change of sign at 60 km, corresponding to the distance of the outcropping of the lower interface. Stability criteria (4) and (5) are not satisfied neither for a two-layer model and for continuous stratification (not shown), showing changes of sign of  $\frac{\partial Q}{\partial y}$  along the thermoclines and thus allowing the system to be baroclinically unstable also for these approximations.

[25] Since that the necessary conditions for stability are not satisfied here, we now analyze the spatial and time scale of the instabilities and we compare the values with the values found in the Scanfish and drifter observations.

## 2.5. Horizontal and Time Scales of the Instabilities

### 2.5.1. First Baroclinic Rossby Radius of Deformation

[26] The preferential length scale at which baroclinic instability occurs is the first baroclinic Rossby deformation radius,  $L_d$ , which is close to the fastest growing mode in the Eady [1949] linear model. Following, for example, Eckart [1969], the first baroclinic Rossby radius can be calculated

using the WKB approximation which assumes that planetary vorticity, stratification and the buoyancy frequency vary slowly on horizontal scales comparable to the Rossby radius of deformation [Gill, 1982], so that  $L_d$  does not depend on the horizontal resolution of the data, as

$$L_d = \frac{1}{f\pi} \int_{-H}^0 N(z) dz, \quad (7)$$

where  $N$  is the buoyancy frequency, with  $N^2 = -\frac{g}{\rho_0} \frac{\partial \sigma}{\partial z}$ ,  $H$  is the depth scale of the mode,  $f$  is the planetary vorticity,  $g$  is gravitational acceleration,  $\sigma$  is potential density and  $\rho_0$  is a reference density.

[27] The first baroclinic Rossby radius of deformation calculated from the Scanfish section shows values increasing from 2 km to 2.5 km as the frontal region is approached, at 50 km distance (Figure 4a, continuous line).  $L_d$  then decreases to 0.5 km over the Dogger Bank, where waters are only weakly stratified. In comparison, using (7), Chelton *et al.* [1998] found typical values of  $L_d$  of 30 km in the open ocean over the midlatitudes.

[28] If instead the system is approximated to a two-layer model, the Rossby radius of deformation can be calculated as

$$L_d = \frac{\sqrt{g'}}{f} \sqrt{\frac{h_1 h_2}{h_1 + h_2}} \quad (8)$$

In the two-layer approximation,  $L_d$  acquires slightly larger values of 3.5 km to 4 km on the deeper regions and decreases to 2 km over the Dogger Bank.

### 2.5.2. Maximum Eady Growth Rate

[29] The characteristic time scale for eddies to be formed by baroclinic instability, is given by the reciprocal of the Eady growth rate maximum,  $\tau_{Eady}^{-1}$ . Following Lindzen and Farrell [1980], the Eady growth rate can be calculated as

$$\tau_{Eady}^{-1} = 0.31 f \sqrt{\frac{1}{H} \int_{-H}^0 \frac{1}{N} \frac{\partial U}{\partial z} dz}, \quad (9)$$

where  $H$  is the total depth of the water column,  $\partial U / \partial z$  is the vertical shear in the horizontal background flow, calculated through thermal wind. In (9) we allow  $N$  to vary with longitude and latitude [Smith, 2007]. The Eady growth rate  $\tau_{Eady}^{-1}$  represents an upper bound for the growth rate of the eddies.

[30] The Eady growth rate shows values increasing from  $0.2 \times 10^{-5} s^{-1}$  to  $1.4 \times 10^{-5} s^{-1}$  corresponding to periods of 6 days to 1 day, as the frontal region is approached (Figure 4b). The values of the Eady growth rate decreases then over the Dogger Bank, reaching a second maxima of  $1.5 \times 10^{-5} s^{-1}$ , corresponding to a period of less than 1 day, on the frontal region corresponding to the grounding of the upper thermocline. In comparison, in the open ocean there are longer typical time scales of  $\tau_{Eady} \sim 15-30$  days [Williams *et al.*, 2007].

## 3. Seasonal Development of the Mesoscale Variability

[31] In the open ocean, the baroclinic instability process acts throughout the year due to the persistent reservoir of

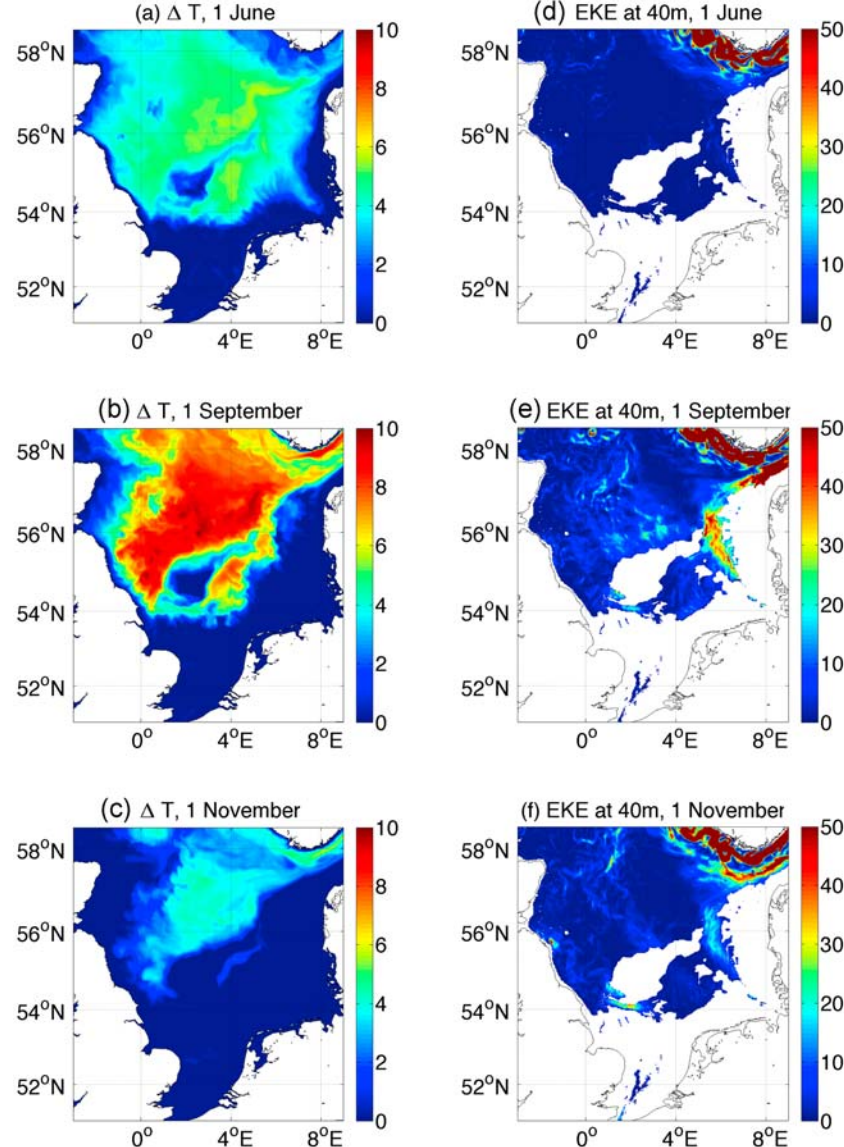


**Figure 5.** Evolution of (a–c) surface to bottom temperature difference ( $^{\circ}\text{C}$ ) and (d–f) eddy kinetic energy per unit volume at 40 m ( $\text{J m}^{-3}$ ) as seen through POLCOMS, for 1 June (Figures 5a and 5d), 1 September (Figures 5b and 5e), and 1 November 2001 (Figures 5c and 5f).

available potential energy associated with the shape of the main pycnocline. There are predicted slight seasonal changes in the baroclinic instability process associated with changes in the velocity shear and instability criteria [Gill *et al.*, 1974]. More importantly, the summer growth of the seasonal pycnocline is expected to increase the baroclinicity and the instability process [Strass *et al.*, 1992].

[32] In the shelf seas, the seasonal changes in stratification are much more severe than in the open ocean: over much of the shelf seas there is no stratification in winter and a seasonal thermocline emerges during the summer. Thus, like Strass *et al.* [1992], we expect that for the shelf seas the baroclinic instability process will be much stronger in summer and absent in winter. There are of course other ways in which fine-scale signals in eddy kinetic energy can be provided: barotropic instability from horizontal shear and transient, stochastic, wind forcing [Frankignoul and Muller, 1979] as well as flow interactions with topography.

[33] To study in detail the seasonal variability and the energetics of the mesoscale activity we will now make use of an eddy-permitting model, the Proudman Oceanographic Laboratory Coastal-Ocean Modelling System (POLCOMS, see Appendix A).

### 3.1. Seasonal Development of Eddy Kinetic Energy

[34] To study the seasonal variability of the mesoscale activity we now consider the regional variations in baroclinicity and EKE variability for three different periods, corresponding to the formation, maximum strength and decay of the stratification (Figure 5). The modeled eddy kinetic energy (EKE) per unit volume is diagnosed at a constant depth of 40 m, i.e., below the surface Ekman layer, as

$$\text{EKE} = \frac{1}{2} \rho (u'^2 + v'^2), \quad (10)$$

where the eddy velocities (prime) are defined as the difference from a 3 month running average with tidal signals removed. The EKE acquires larger values in the Norwegian Trench and at the frontal region which separates the stratified to the well-mixed regions of the domain. In the Norwegian Trench, the EKE per unit volume acquires large values throughout the entire year, while at the frontal region, the EKE per unit volume is zero at the formation of the stratification (Figures 5a and 5d), reaches  $35 \text{ J m}^{-3}$  when the stratification is at its maximum strength (Figures 5b and 5e) and decays to  $20 \text{ J m}^{-3}$  at the stratification weakens (Figures 5c and 5f). High values of EKE are present in the form of filaments with a wavelength comparable to the local values of the modeled first baroclinic Rossby radius of deformation.

### 3.2. Stability of the Modeled Fronts

[35] Given the seasonal development of the modeled EKE, the necessary conditions for stability (4) and (5) are examined for the numerical model in the same location of the high-resolution Scanfish section. The modeled potential vorticity is calculated as  $PV = -\left(\frac{f+\xi}{\rho_0}\right)\frac{\partial \sigma}{\partial z}$ , where  $\xi = \frac{\partial v}{\partial x} - \frac{\partial u}{\partial y}$  is the vertical component of the relative vorticity. North of the Dogger Bank the Rossby number reaches maximum values of 0.3 along eddy filaments when the stratification reaches its maximum, hence the contribution of the relative vorticity is relatively small.

[36] In the period of maximum stratification, the density field (Figure 6a) shows the presence of a double thermocline structure, which allows the system to be approximated as a three layer problem. The necessary conditions for stability (4) and (5) for the three layer problem are violated (Figures 6c–6f) allowing the process of baroclinic instability. The potential vorticity field (Figure 6b) follows mainly the upper thermocline, where it shows a marked variability implying changes in the sign of the potential vorticity gradient also for continuous stratification.

[37] At the onset and decay of the stratification, there is a sharp thermocline, which allows the system to be approximated to a two layer problem (Figures 7a and 7b). Using the two layer approximation, there is a change of sign of  $\bar{u}_i \frac{\partial Q_i}{\partial y}$  and  $\frac{\partial Q_i}{\partial y}$  (Figures 7c–7f), permitting baroclinic instability from (4) and (5). There is also a marked variability in the potential vorticity (Figures 7a and 7b), which likewise implies changes in the sign of the potential vorticity gradient for continuous stratification.

[38] Even if the necessary conditions for stability appear to be always violated in all the three periods, the EKE shows a marked seasonal variability (Figure 5). In section 3.3, the question on how is this variability controlled is addressed studying the energetics of the problem.

### 3.3. How Is the Eddy Seasonal Variability Controlled?

[39] To study how the mesoscale variability is forced, the time evolution of the modeled eddy kinetic energy (EKE) per unit volume is diagnosed at a constant depth of 40 m, i.e., below the surface Ekman layer, and along the summer thermocline. Fields are spatially averaged over the southern North Sea frontal regional,  $0^\circ\text{E}$  to  $7^\circ\text{E}$  and  $54^\circ\text{N}$  to  $57^\circ\text{N}$  subdomain, as well as further time-averaged over a 3 day running average, where the 3 days period corresponds to the Eady growth period approximating to the frontal region

(Figure 4b). Both the subsurface and thermocline EKE per unit volume show a peak in late summer and early autumn, around day 270, rather than during winter, with values of the order of 10 to  $15 \text{ J m}^{-3}$  (Figures 8a and 8b).

[40] In comparison, the rate of wind energy input is calculated as [e.g., Wunsch, 1998]

$$W = \vec{\tau} \cdot \vec{u}, \quad (11)$$

where  $\vec{\tau}$  is the wind stress, following Smith and Banke [1975] and  $\vec{u}$  is the surface geostrophic current. The daily wind energy input per unit volume shows local peaks occurring throughout the year linked to the passage of synoptic weather systems (Figure 8c). The wind energy input per unit volume is relatively small over a single day. However, to compare with the EKE, the wind input is integrated over 3 months, which is comparable with the period of persistence of the maximum stratification and can thus probably be viewed as an upper bound for the likely storage. The 3 months integrated wind input shows that wind energy might be the source of mesoscale variability during winter, when the wind stress energy per unit volume shows peaks of about  $5 \text{ J m}^{-3}$  to  $8 \text{ J m}^{-3}$  and a mean value of the order of  $2 \text{ J m}^{-3}$ , which is in agreement with the mean value of the subsurface EKE (Figure 8d). The wind energy per unit volume shows a second peak in late autumn, that follows the peak of the subsurface EKE. Hence, local peaks in EKE throughout the year might reflect the passage of synoptic weather systems. However, in late summer, the wind energy input over 3 months shows values only of the order  $2 \text{ J m}^{-3}$ , compared with an EKE of 10 to  $15 \text{ J m}^{-3}$ . Hence, this difference between the values of the wind energy input over 3 months and the EKE suggests that there are other EKE sources.

[41] Now consider the seasonal variation of the baroclinicity, represented from the available potential energy per unit volume, calculated as

$$APE = \frac{\rho_0 f^2}{6 H} \int_V \frac{1}{N} \frac{\partial U}{\partial z} dx dy dz. \quad (12)$$

where  $V$  is the volume of the domain considered. Note the direct proportionality between the APE per unit volume and  $\tau_{Eady}^{-2}$ . The APE per unit volume shows a peak around day 270, which correspond to the maximum in the subsurface and thermocline EKE per unit volume (Figure 8e). The lack of a phase lag between the peaks in the EKE and APE is in agreement with baroclinic instability theory: in the coastal ocean the expected phase lag would be the order of 1 to 6 days, as based upon the diagnosed Eady growth period. For comparison, in the open ocean, a phase lag between the maximum in the baroclinicity and the EKE of 1 to 2 months might be expected [Williams et al., 2007]. The variability of the subsurface and thermocline EKE appears thus to be affected by the baroclinicity of the shelf seas, which might provide the energy for the development of mesoscale variability, as well as by the external wind forcing.

[42] Notice that, in contrast to the APE, the surface to bottom temperature difference (Figure 8f) increases in early spring, reaches a maximum in summer of  $\Delta T = 7^\circ\text{C}$  around day 190, and then is eroded in late autumn and removed in

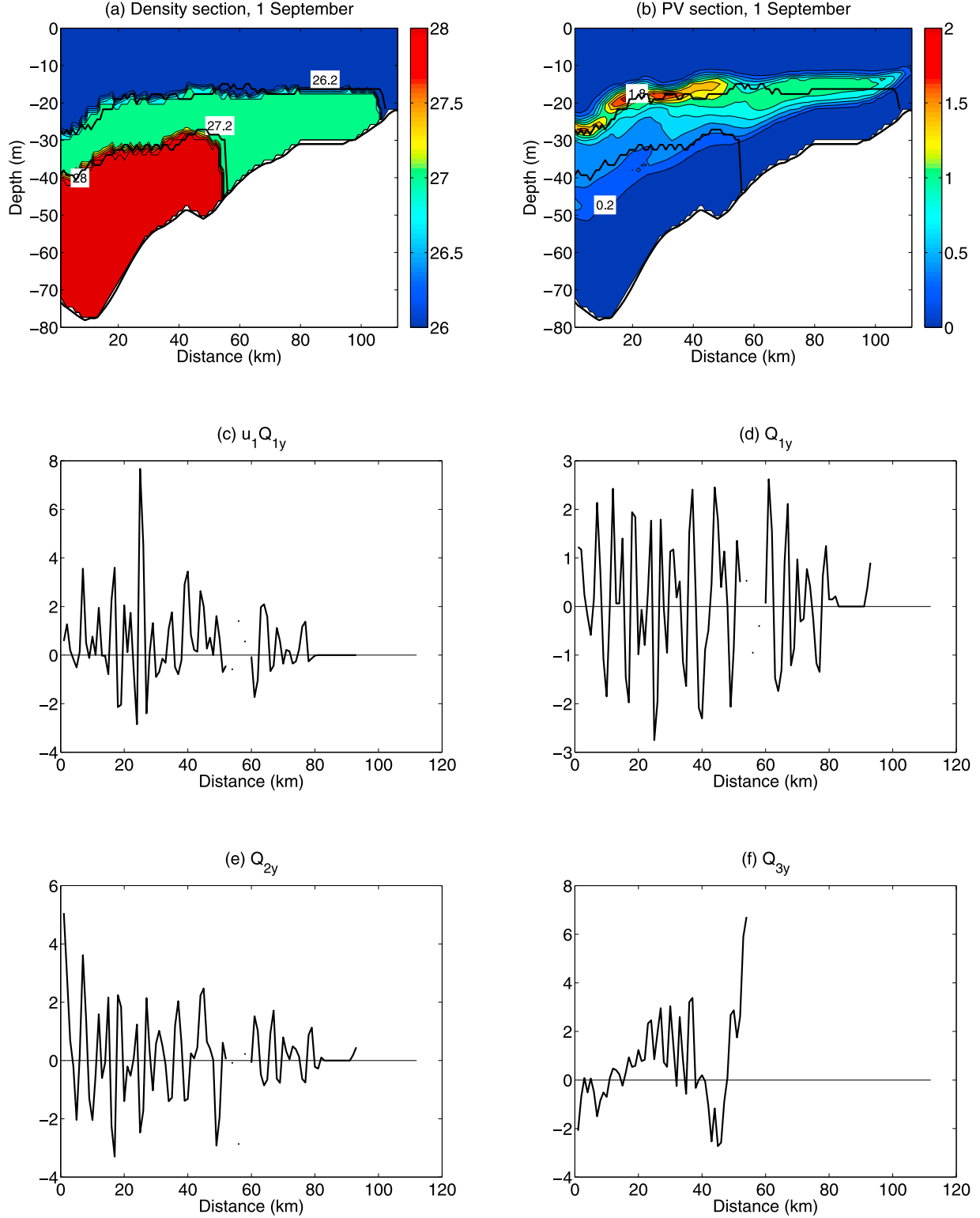


**Figure 6.** (a) The  $\sigma$  density and (b) PV ( $\text{m}^{-1} \text{s}^{-1}$ ) sections for 1 September as seen through POLCOMS. The thick black lines represent the interfaces for the three-layer approximation. (c–f) Stability criteria analysis for 1 September for the three-layer approximation. South is to the right.

winter. The phase lag between the modeled APE and the surface to bottom temperature difference is due to the evolution of the vertical shear of the mean current and of the sharpening of the thermocline, affecting the  $N^2$  profile.

Hence, there is a seasonal evolution of EKE, probably reflecting the effect of different sources.

[43] There is a positive correlation between low EKE and APE in the late winter and spring period, and a peak of high

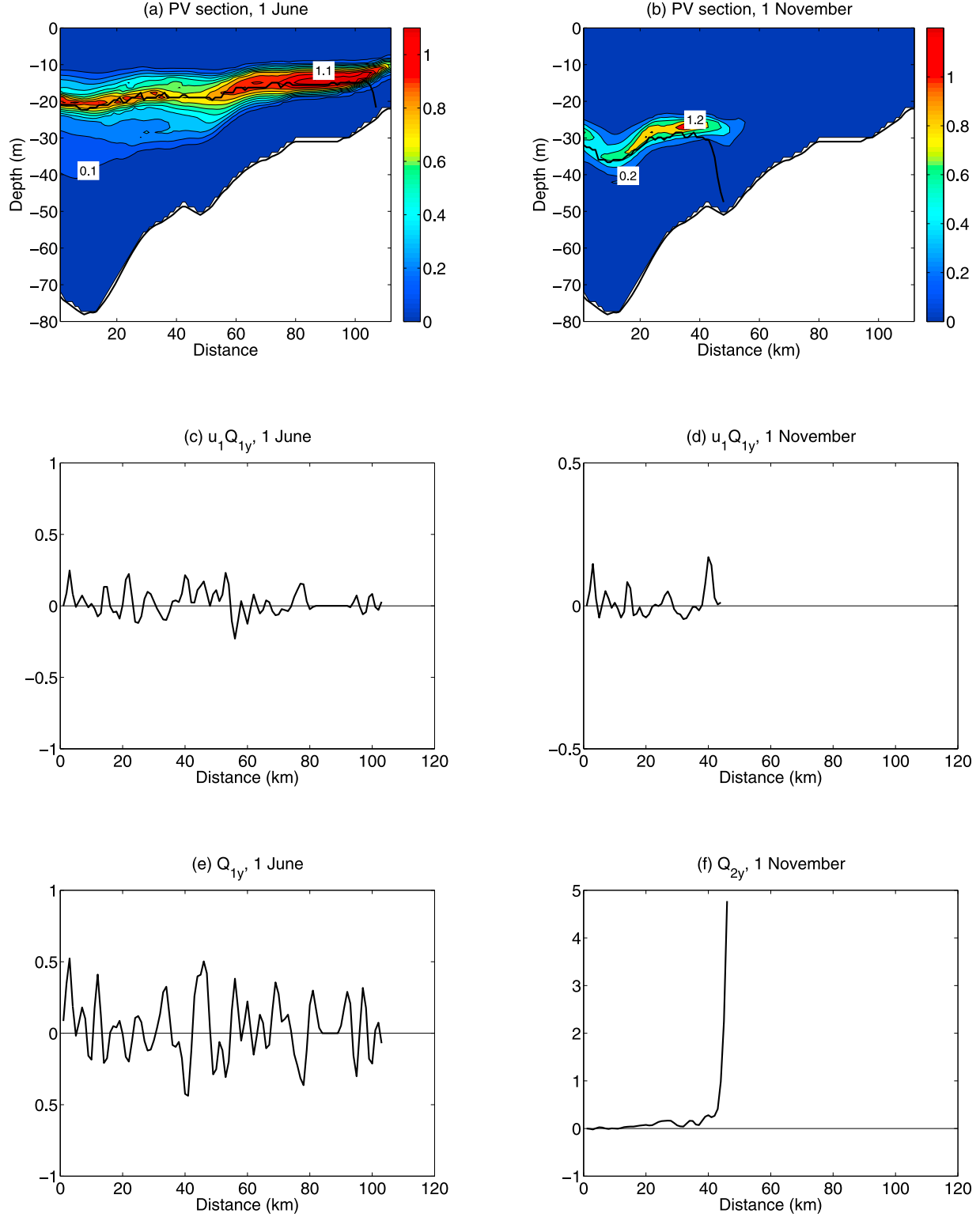


**Figure 7.** PV ( $\text{m}^{-1} \text{s}^{-1}$ ) sections for (a) 1 June and (b) 1 November as seen through POLCOMS. The thick black lines represent the interface for the two-layer approximation. (c–f) Stability criteria analysis for 1 June (Figures 7c and 7e) and 1 November (Figures 7d and 7f) for the two-layer approximation. South is to the right.

EKE and APE for the early autumn (Figure 9a, where the color of the dots indicate the day of the year). The EKE shows instead a less clear relationship with the wind energy input integrated over 3 months (Figure 9b): the two quan-

tities show an approximately linear relationship. EKE shows a peak in the early autumn, which corresponds to low values of wind energy input.

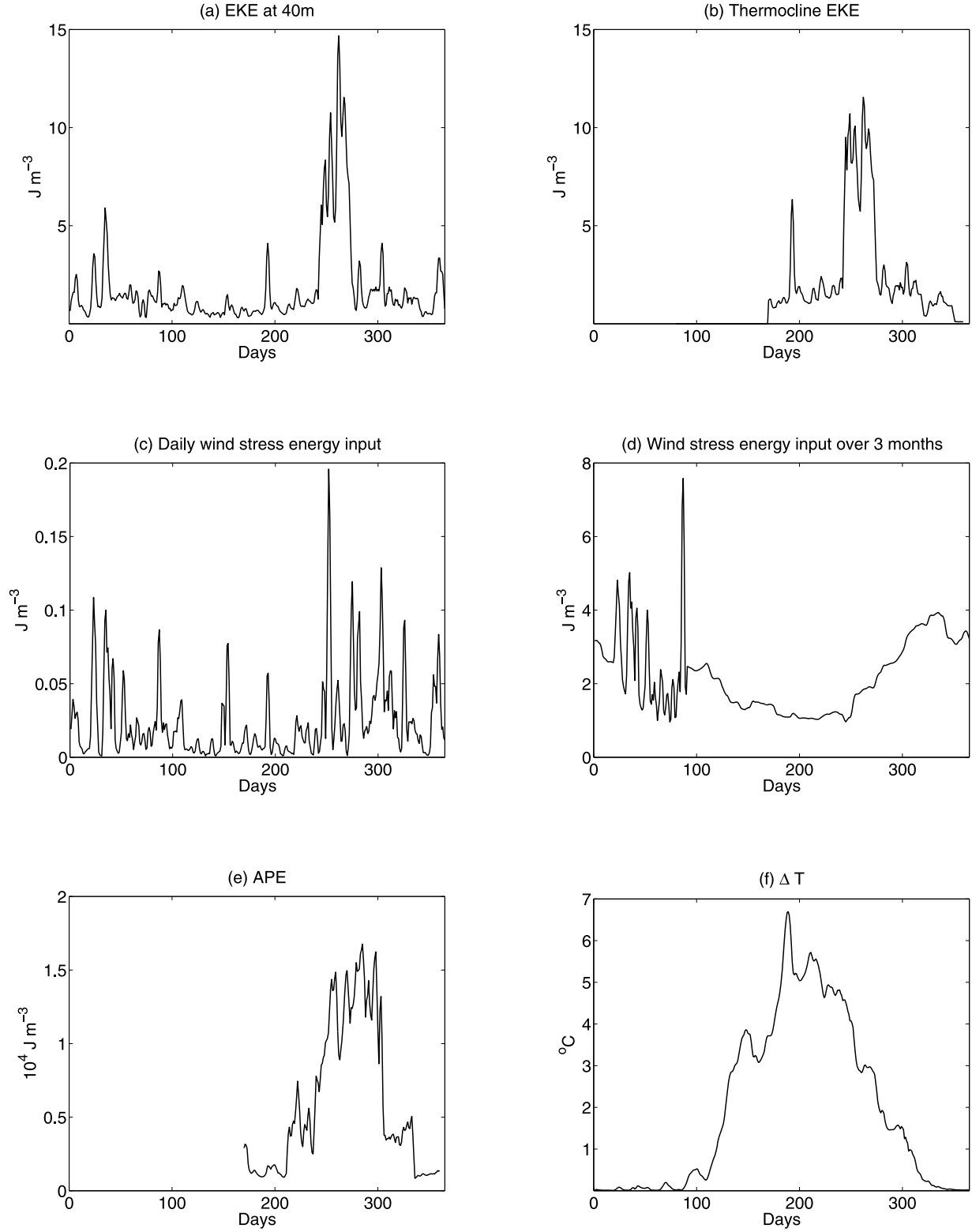


**Figure 8.** Time evolution of 5 day running averages of eddy kinetic energy per unit volume ( $J \text{ m}^{-3}$ ) (a) at 40 m and (b) along the summer thermocline, (c) daily wind energy per unit volume ( $J \text{ m}^{-3}$ ), (d) wind energy input per unit volume ( $J \text{ m}^{-3}$ ) over 3 months, (e) available potential energy per unit volume ( $10^4 J \text{ m}^{-3}$ ), and (f) surface to bottom temperature difference ( $^{\circ}\text{C}$ ). The area average is calculated in the  $0^{\circ}\text{E}$  to  $7^{\circ}\text{E}$  and  $54^{\circ}\text{N}$  to  $57^{\circ}\text{N}$  subdomain, which includes the southern North Sea frontal region. The EKE along the summer thermocline and the APE are calculated from the summer to the late autumn, when the stratification is stronger.

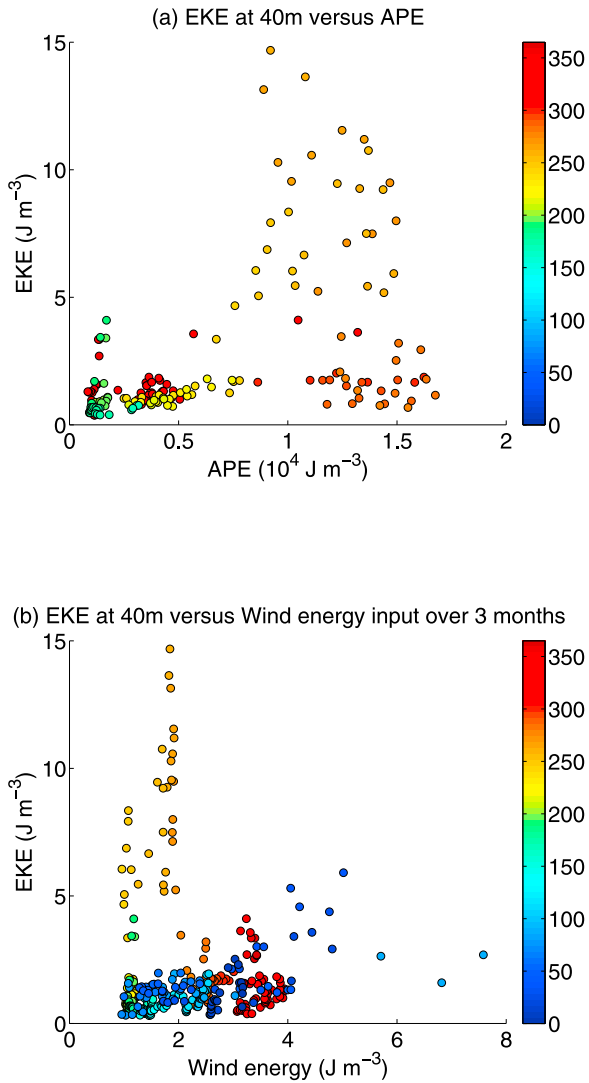


**Figure 9.** Relations between (a) eddy kinetic energy per unit volume ( $\text{J m}^{-3}$ ) at 40 m and available potential energy ( $10^4 \text{ J m}^{-3}$ ) and (b) eddy kinetic energy per unit volume at 40 m and wind energy input over 3 months ( $\text{J m}^{-3}$ ) for the  $0^\circ\text{E}$  to  $7^\circ\text{E}$  and  $54^\circ\text{N}$  to  $57^\circ\text{N}$  subdomain. Colors indicate days of the year.

[44] Given that baroclinicity might be playing an important role in controlling the EKE variability, now consider how the energy is partitioned.

### 3.4. Ratio of EKE/APE

[45] Following linear instability theory [Gill *et al.*, 1974], the ratio between the eddy kinetic energy and available potential energy is given by

$$\frac{EKE}{APE} = (kL_d)^2, \quad (13)$$

where  $k$  is the eddy wave number. This ratio is expected to be of order  $10^3$  at the large scale and of order 1 when the growing modes have an inverse wave number comparable to the deformation radius,  $k^{-1} \sim L_d$ .

[46] At large scale, defined by an area integration over the southern North Sea ( $0^\circ\text{E}$  to  $7^\circ\text{E}$  and  $54^\circ\text{N}$  to  $57^\circ\text{N}$ ), this ratio is of order  $1.5 \times 10^3$  in late summer (Figures 8a, 8b, and 8e), in agreement with baroclinic instability theory.

[47] Now consider how the APE varies on the eddy scales (1–5 km). At these eddy scales, for shelf sea fronts, the available potential energy is also linked with the potential energy anomaly [Simpson and Hunter, 1974]

$$\phi = \frac{1}{h} \int_{-h}^{\zeta} (\bar{\rho} - \rho) g z dz, \quad (14)$$

where  $\phi$  is the work per unit volume required to bring a mass of stably stratified water to a vertically mixed state: for a vertically mixed system  $\phi = 0$ , while for increasingly stable stratification  $\phi > 0$ , and for statically unstable conditions,  $\phi < 0$ ;  $\bar{\rho}$  is the depth mean density. At the frontal region the eddy potential energy anomaly is an upper limit to the available potential energy: if this is not the case, eddies would restratify the frontal region.

[48] Keeping this upper limit in mind, for a two layer system the APE can be written as

$$APE = -\phi' + \frac{1}{2} g' \rho_2 \frac{H_2}{H} h'_1 \quad (15)$$

where the first term on the r.h.s.,  $\phi'$ , is the eddy potential energy anomaly, and the second term is the potential energy associated to the layer thickness anomaly  $h'_1$  (see Appendix B); where  $g'$  is the reduced gravity of the system. For an eddy transferring well-mixed waters into the stratified region of a shelf sea front, the APE signal is linked to  $\phi' < 0$  and  $h'_1 > 0$ .

[49] For simplicity, ignore the advection of the layer thickness anomaly, and assume that the available potential energy per unit volume is approximated by the eddy potential energy anomaly. Then, applying the typical frontal values of  $EKE = 30 \text{ J m}^{-3}$  (Figure 5e) and approximated  $APE \approx -\phi' = 25 \text{ J m}^{-3}$  (not shown) gives  $EKE/APE \approx 1$ , which is in accord with the ratio expected from baroclinic instability theory on the eddy scale. In addition, assuming (13) and our previously diagnosed frontal value of  $L_d = 1 \text{ km}$  implies a characteristic wavelength  $\lambda = 6.3 \text{ km}$ . This length scale is in agreement with the sizes of the eddy motion detected by the drifter analysis (Figure 2) and of the freshwater intrusion observed by the Scanfish section (Figure 1b). Thus, both the ratio of  $EKE/APE$  on the eddy scale and the length scales appear to be consistent with the eddies being generated by baroclinic instability.

### 3.5. Modeled Rossby Radius of Deformation and Eady Growth Rate

[50] The modeled Rossby radius of deformation and Eady growth rate are diagnosed for the three different periods, corresponding to the formation, maximum strength and decay of the stratification, as in section 3.1.

[51] The modeled first baroclinic Rossby radius of deformation shows a seasonal variability that follows the seasonal variability of the stratification (Figures 10a–10c).

[52] At the maximum of the stratification, for continuous stratification  $L_d$  varies from less than 1 km in the proximity of the well-mixed region, increasing to  $O(<3 \text{ km})$  in the

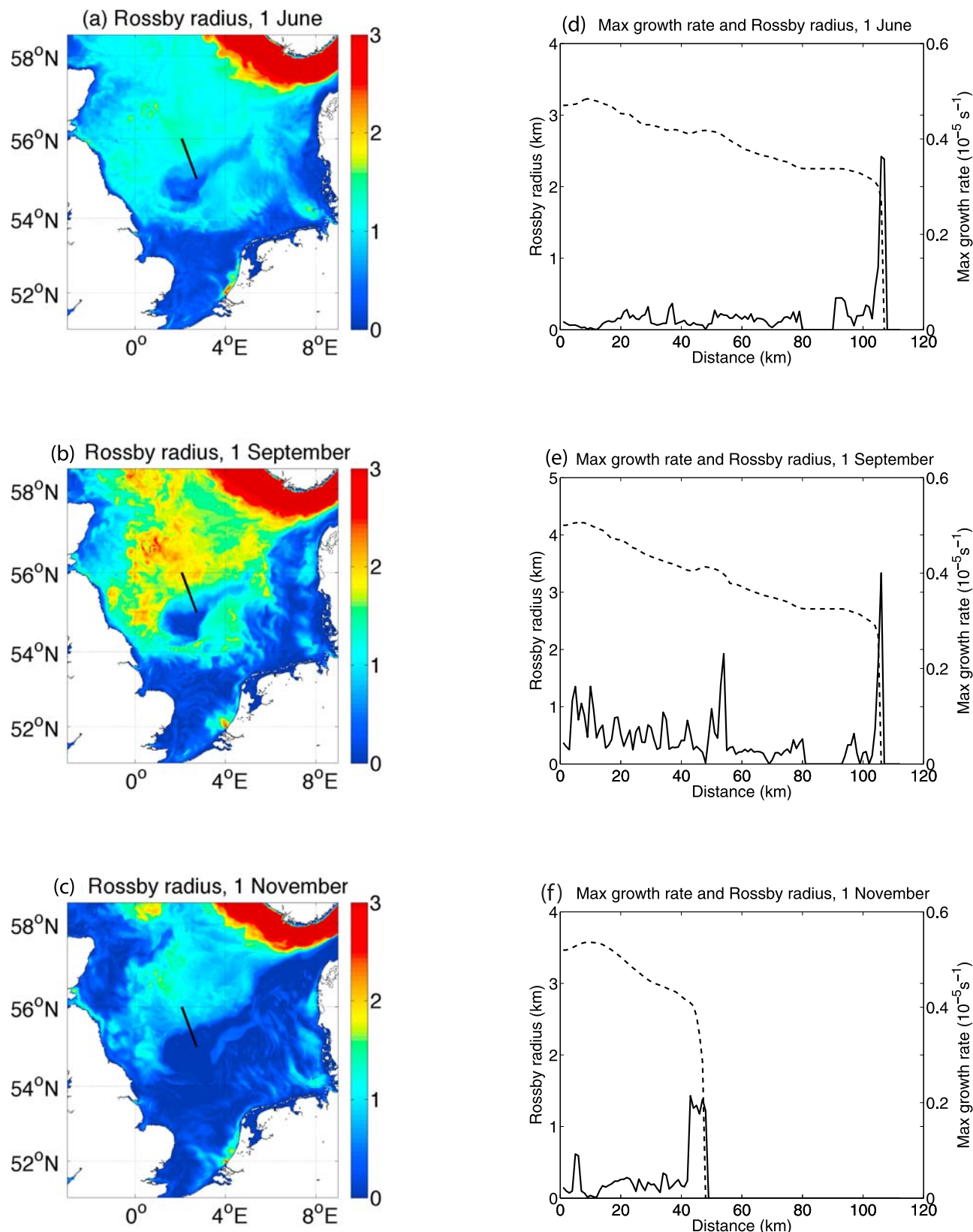


**Figure 10.** (a–c) Time evolution of the first baroclinic Rossby radius of deformation (km). Thick black line indicates the position of the vertical section. (d–f) Time evolution of the two-layer Rossby radius of deformation (km, dashed line) and maximum Eady growth rate ( $\text{s}^{-1}$ , continuous line) along the vertical section as seen through POLCOMS. South is to the right. Figures 10a and 10d are for 1 June, Figures 10b and 10e are for 1 September, and Figures 10c and 10f are for 1 November.

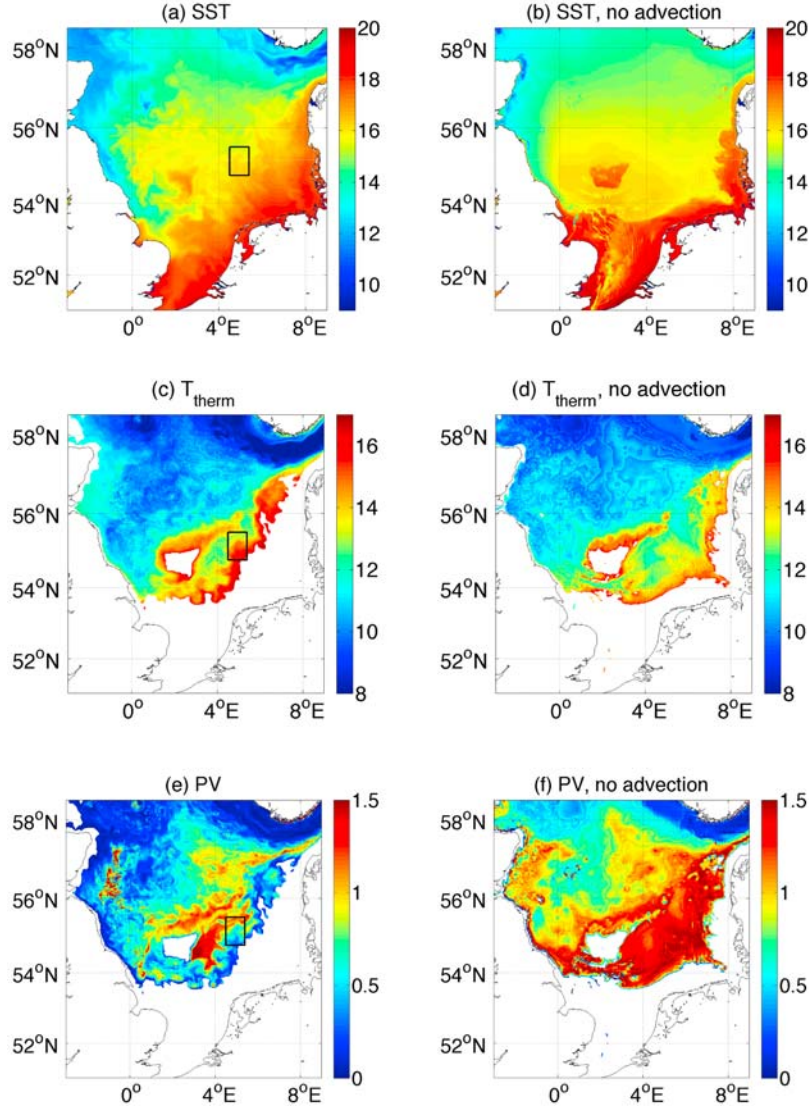


**Figure 11.** POLCOMS (a) sea surface temperature ( $^{\circ}\text{C}$ ), (b) sea surface temperature without advection, (c) thermocline temperature, (d) thermocline temperature without advection, (e) thermocline potential vorticity ( $10^{-8} \text{ m}^{-1} \text{ s}^{-1}$ ), and (f) thermocline potential vorticity without advection for 1 September 2001. White region indicates where the thermocline outcropped or grounded. The square shows the position of the eddy analyzed in Figure 12.

central and northern North Sea and reaching larger values of  $O(>3 \text{ km})$  along the Norwegian Trench (Figure 10b), while for the two-layer approximation, applied along the vertical section north of the Dogger Bank,  $L_d$  varies from 2 km in the proximity of the frontal region, increasing to 4 km in the central part of the domain (Figure 10e, dashed line). The model estimates are comparable to the diagnostics from the Scanfish section, ranging from 0.5 km over the Dogger Bank and increasing to 2 to 2.5 km in more stratified waters for the continuous stratification and from 2 km over the Dogger Bank and increasing to 3.5 km in more stratified waters for the two-layer approximation (Figure 4a).

[53] The Eady growth rate, calculated along the vertical section north of the Dogger Bank, shows also a seasonal variability that follows the seasonal variability of the stratification (Figures 10d–10f, continuous lines). At the maximum of the stratification, the Eady growth rate (Figure 10e) reaches values of  $0.4 \times 10^{-5} \text{ s}^{-1}$  at the frontal region,

corresponding to a period of 3 days, and decreases  $0.1 - 0.2 \times 10^{-5} \text{ s}^{-1}$ , to corresponding to a period of 6–11 days, in the central part of the domain. Again, these time scales are comparable to the short Eady growth periods of 1 to 6 days diagnosed from the Scanfish data (Figure 4b).

#### 4. What Are the Effects of the Eddies in the Shelf Seas?

[54] Given the energetic analysis, now consider the effect of the modeled eddies. The sea surface temperature reveals warm waters in the southern part of the domain, corresponding to the well-mixed region, with small-scale filaments propagating in the center of the domain where waters are stratified (Figure 11a). Along the thermocline, the modeled temperature shows the presence of warm water intrusions from the well-mixed to the stratified region (Figure 11c). The eddy origin of the intrusions is suggested

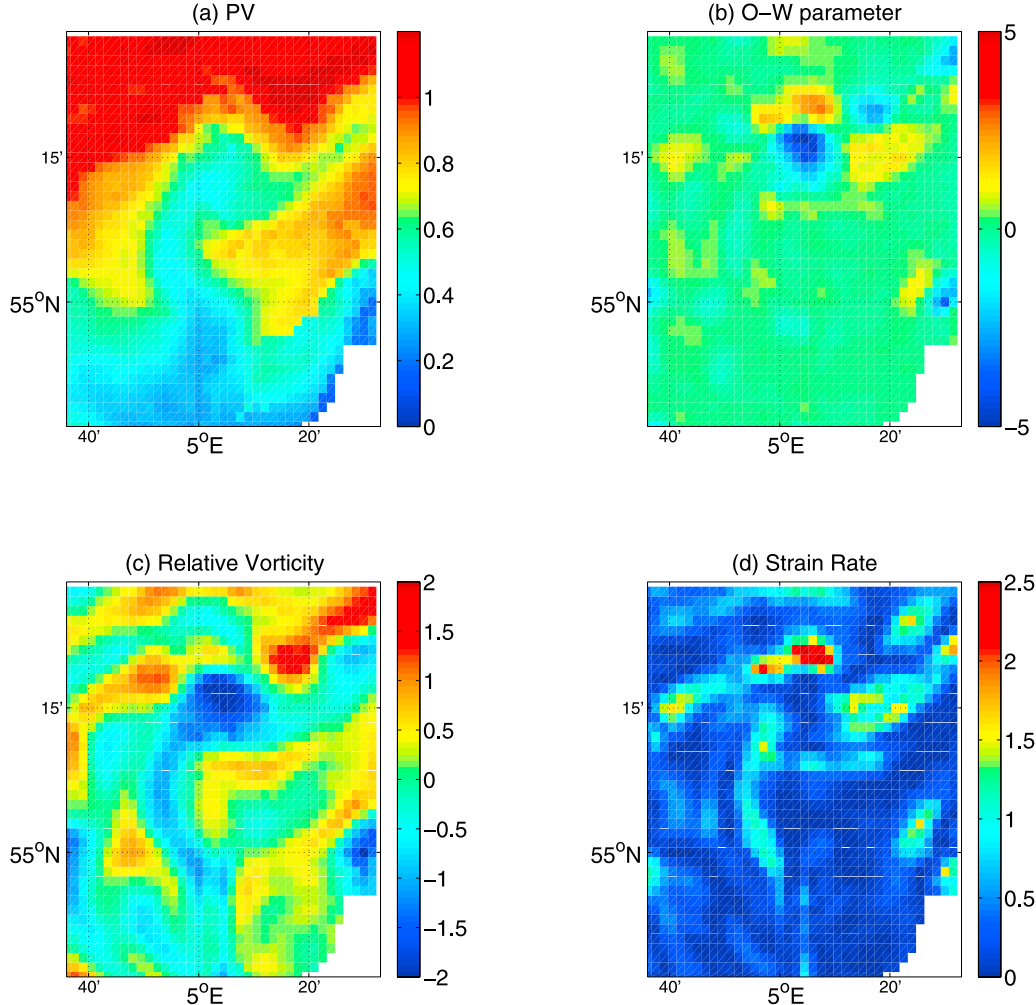


**Figure 12.** POLCOMS (a) PV ( $10^{-8} \text{ m}^{-1} \text{ s}^{-1}$ ), (b) Okubo-Weiss parameter ( $10^{-10} \text{ s}^{-2}$ ), (c) relative vorticity ( $10^{-5} \text{ s}^{-1}$ ), and (d) strain rate ( $10^{-10} \text{ s}^{-1}$ ) for an eddy centered at  $55^\circ\text{N}$ ,  $5^\circ\text{E}$  for 1 September 2001.

by the low potential vorticity, which is a signature of the well-mixed waters (Figure 11e).

[55] The eddy nature of the intrusions is also revealed in idealized model thought experiments where the scalar advection is artificially turned off. The lack of scalar advection inhibits the formation of baroclinic instabilities due to the nonadjustment of the density field under the action of thermal wind, as well as reducing vertical mixing [Holt and Umlauf, 2008] leading to stronger stratification. In the absence of scalar advection, fronts behave like barriers, and the mesoscale filaments propagating from the well-mixed to the stratified region disappear (Figures 11a and 11b, respectively). There is an absence of any transfer of warm waters (Figures 11c and 11d) and low potential vorticity from the well-mixed to the stratified regions (Figures 11e and 11f). In contrast, when there is scalar advection, there are mesoscale filaments and fluxes of low potential vorticity along the thermocline, where they are connected to coherent eddies (Figure 11e).

[56] An analysis of the dynamical regimes in the frontal regions can be made using the Okubo-Weiss parameter [Okubo, 1970; Weiss, 1991],

$$OW = s^2 - \xi^2 \quad (16)$$

where  $s^2 = (\frac{\partial u}{\partial x} - \frac{\partial v}{\partial y})^2 + (\frac{\partial v}{\partial x} - \frac{\partial u}{\partial y})^2$  is the square of the strain (or deformation) rate  $s$  and  $\xi$  is the vertical component of the relative vorticity. Analyzing a modeled eddy propagating along the thermocline (Figure 12a), see the area enclosed in the square in Figures 11a, 11c, and 11e),  $OW$  allows the partition of the domain into two regimes: vorticity dominated regions ( $OW < 0$ , Figures 12b and 12c), usually associated with the vortex cores and where tracer gradients are expected to rotate without growing or decreasing; and strain dominated regions ( $OW > 0$ ), within filaments between eddies (Figures 12b and 12d), where vorticity is strongly sheared by the strain and the dynamics are dominated by chaotic stirring [Bardin, 2007]. For shelf sea eddies, vorticity represents then a barrier to mixing within the core of the eddies, but there is enhanced strain between eddies.

## 5. Discussion

[57] The role of baroclinic instability in the shelf sea is examined using a combined study of high-resolution synoptic observations and eddy-permitting modeling for the North Sea. The study addresses if geostrophic eddies are formed by baroclinic instability along tidal fronts in shelf

seas, separating well mixed and stratified waters. Possible eddy signals are indicated in high-resolution Scanfish sections along the thermocline, with freshwater intrusions on the eddy scale. Drifters data reveal circulating trajectories, consistent with mesoscale eddies.

[58] Stability analysis of the frontal system shows that eddies might be formed by baroclinic instability. The low potential vorticity of the low-salinity water intrusions suggest that they originate from where the thermocline outcrops in the well-mixed region. High-resolution analysis of the Rossby deformation radius and maximum Eady growth rate suggest that the eddies in the shelf seas have small horizontal scales, decreasing from 4 km in the stratified region to 2 km at the frontal region, and have short formation time scales, decreasing from 6 days in the stratified region to 1 day at the frontal region.

[59] Eddy-permitting model investigations reveal how there is greater eddy kinetic energy during the late summer and early autumn, when the baroclinicity is strong, allowing the vertical reversal of the isopycnic potential vorticity gradient, as assessed from the stability analysis of the modeled fronts and in agreement with *Strass et al.* [1992]. Energy analysis reveals that the wind energy input is not high enough to explain the values of the eddy kinetic energy in the interior during summer, but can be important during winter/spring. The ratio of the eddy kinetic energy and the available potential energy for the summer period is also consistent with baroclinic instability theory, which predicts that the ratio should be of  $O(10^3)$  at the large scale and of  $O(1)$  at the eddy scale.

[60] At the eddy scales there can be regions of high stirring between the eddies, due to the high strain rates, and reduced stirring within the eddies, due to their high vorticity. The eddies can play an important role in the lateral transfer of tracers across fronts in shelf seas: in particular, eddies may transfer low stratification and potential vorticity from well mixed waters across a shelf front along the thermocline into the stratified interior (Figure 11). Accompanying this dynamic transfer, there is likely to be an associated transfer of passive tracers, such as nutrient-rich, well-mixed waters transferred to nutrient-depleted stratified waters. Being nutrient-rich and with reduced stirring, the regions within the eddies can, thus, be favorable for biological production, as suggested by the increased fluorescence in the high-resolution Scanfish section (Figure 1f). This eddy transfer might then be an important complement to diapycnal mixing [*Sharples et al.*, 2001] in sustaining the nutrient budget in stratified waters of the shelf seas and in the transfer of  $CO_2$  [*Thomas et al.*, 2004], as has been discussed for the open ocean [*Williams and Follows*, 2003].

## Appendix A

[61] POLCOMS (Proudman Oceanographic Laboratory Coastal-Ocean Modelling System) is employed is a three-dimensional baroclinic finite difference model, based on a B grid, on spherical polar s coordinates [*Song and Haidvogel*, 1994], with prognostic temperature and salinity, and using the “Piecewise Parabolic Method” as advection scheme [*James*, 1996]. A complete description is given by *Holt and James* [2001], so that just the general characteristics of the model will be reported here. The model is forced by

6-hourly ECMWF atmospheric data model. Surface fluxes are prescribed through bulk formulae [*Smith and Banke*, 1975; *Gill*, 1982]. Boundary data are provided by POLCOMS Atlantic Margin Model, with a resolution of 12 km. The POLCOMS Atlantic Margin Model, in turn, is forced by the North Atlantic FOAM Model [*Bell et al.*, 2000]. A flux/radiation scheme for the barotropic component and an upwind advection scheme for temperature and salinity are used at the open boundaries. Boundary data consist of hourly elevations and depth mean currents, and daily depth-varying currents temperature and salinity. The river database includes 300 rivers discharging into the domain, gauged up to daily frequency. POLCOMS employ a Mellor-Yamada-Galperin level 2.5 turbulence closure scheme [*Mellor and Yamada*, 1974; *Galperin et al.*, 1988] implemented with the use of an algebraic mixing length. The model includes both momentum and scalar diffusion, with Laplacian horizontal turbulent diffusivity on s levels calculated following *Smagorinsky* [1963]. The model is integrated in the North West European Shelf, extending over a domain of  $-12^\circ E$  to  $10^\circ E$  and  $48^\circ N$  to  $64^\circ N$ , with the open boundary following the 200 m isobath, except for where it intersects the deeper Norwegian Trench [*Holt and Proctor*, 2008]. However, only a smaller selection of the domain, corresponding to the Southern and Central North Sea region,  $-3^\circ E$  to  $9^\circ E$  and  $51^\circ N$  to  $58.5^\circ N$ , is diagnosed here (Figure 1a). The model resolution is  $(\frac{1}{40})^\circ$  in longitude and  $(\frac{1}{60})^\circ$  in latitude, corresponding to a grid spacing of  $\approx 1.6$  km and  $\approx 1.8$  km respectively, with a vertical resolution of 34 s levels. The model is initialized from rest, starting on the 1 January 2001 and integrated for one year, until the 31 December 2001. Daily mean fields are obtained through 25 h averaging to remove tidal signals.

## Appendix B

[62] In order to study the relationship between the potential energy anomaly and the available potential energy, consider a two-layer ocean with layers densities  $\rho_1$  and  $\rho_2$  ( $\rho_1 < \rho_2$ ), a flat bottom, rigid lid and total depth  $H = h_1 + h_2$ , where the vertically averaged density is

$$\bar{\rho} = \frac{1}{H} [\rho_1 h_1 + \rho_2 (H - h_1)], \quad (B1)$$

and the potential energy anomaly (14) becomes

$$\phi = -\frac{1}{2} \frac{h_1^2}{H} g(\rho_2 - \rho_1) + \frac{1}{2} g h_1 (\rho_2 - \rho_1). \quad (B2)$$

Decomposition into mean and eddy (indicated with a prime) components

$$\phi = \Phi + \phi', h_1 = H_1 + h'_1, h_2 = H_2 + h'_2 \quad (B3)$$

where  $H_1 + H_2 = H$ , gives

$$\phi' = -\frac{g'}{2} \rho_2 \left( \frac{h_1'^2}{H} - \frac{H_2}{H} h'_1 \right) \quad (B4)$$

where  $g' = g \frac{(\rho_2 - \rho_1)}{\rho_2}$  is the reduced gravity of the system. The first term in the right-hand side of (B4) is the available potential energy per unit volume [*Lorenz*, 1955]

$$APE = \frac{1}{2} g' \rho_2 \frac{h_1'^2}{H} \quad (B5)$$

and is linked to the slope of the isopycnals, while the second term represents the potential energy per unit volume associated with the layer thickness anomaly. Equation (B4) sets the relationship between the available potential energy and eddy potential energy anomaly:

$$APE = -\phi' + \frac{1}{2}g'\rho_2 \frac{H_2}{H} h'_1. \quad (\text{B6})$$

[63] The first term on the right-hand side of (B4) is of  $O(\frac{h^2}{H})$ , while the second term is of  $O(h'_1)$ . Since the ratios of the first two terms on the right-hand side of (B4) is of  $O(\frac{h'_1}{H_2}) \ll 1$ , the eddy potential energy anomaly is not dominated by the available potential energy, but is instead controlled by the layer thickness anomaly through the term  $\frac{1}{2}g'\rho_2 h'_1$ .  $\phi'$  represents thus an upper bound to the available potential energy in the frontal region. Note that for eddies transferring properties from the well-mixed to the stratified region  $\phi' < 0$  and  $h'_1 > 0$ . The tracer-like advection by eddies of the potential energy anomaly sets then the role of the eddies in transferring low stratification from the well-mixed to the stratified side of the fronts.

[64] **Acknowledgments.** G.B. was supported by a CEFAS grant, the Proudman Oceanographic Laboratories, and the UK Natural Environment Research Council (NE/D011108/1). We thank two anonymous referees for constructive comments, which strengthened the study.

## References

- Armi, L., and W. Zenk (1984), Large lenses of highly saline Mediterranean Water, *J. Phys. Oceanogr.*, **14**, 1560–1576.
- Bardin, G. (2007), Are eddies important in the coastal ocean? A North Sea case study, Ph.D. thesis, 238 pp., Univ. of Liverpool, Liverpool, U. K.
- Barth, J. A. (1989a), Stability of a coastal upwelling front: 1. Model development and a stability theorem, *J. Geophys. Res.*, **94**, 10,844–10,856.
- Barth, J. A. (1989b), Stability of a coastal upwelling front: 2. Model results and comparison with observations, *J. Geophys. Res.*, **94**, 10,857–10,883.
- Barth, J. A., S. D. Pierce, and T. J. Cowles (2005), Mesoscale structure and its seasonal evolution in the northern California Current System, *Deep Sea Res., Part II*, **52**, 5–28.
- Bell, M. J., R. M. Forbes, and A. Hines (2000), Assessment of the FOAM global data assimilation system for real time operational ocean forecasting, *J. Mar. Syst.*, **25**, 1–22.
- Brown, J., A. E. Hill, L. Fernand, and K. J. Horsburgh (1999), Observations of a seasonal jet-like circulation at the central North Sea cold pool margin, *Estuarine Coastal Shelf Sci.*, **48**, 343–355.
- Brown, J., L. Fernand, K. J. Horsburgh, A. E. Hill, and J. W. Read (2001), Paralytic shellfish poisoning on the east coast of the UK in relation to seasonal density-driven circulation, *J. Plankton Res.*, **23**, 105–116.
- Bryden, H. (1979), Poleward heat flux and conversion of available potential energy in Drake Passage, *J. Mar. Res.*, **37**, 1–22.
- Castelao, R. M., T. P. Mavor, J. A. Barth, and L. C. Breaker (2006), Sea surface temperature fronts in the California Current System from geostationary satellite observations, *J. Geophys. Res.*, **111**, C09026, doi:10.1029/2006JC003541.
- Charney, J. G., and M. E. Stern (1962), On the stability of internal baroclinic jets in a rotating atmosphere, *J. Atmos. Sci.*, **19**, 159–172.
- Chelton, D. B., R. A. deSzoeke, M. G. Schlax, K. El-Naggar, and N. Siwertz (1998), Geographical variability of the first baroclinic Rossby radius of deformation, *J. Phys. Oceanogr.*, **28**, 433–460.
- D’Asaro, E. A. (1988), Generation of submesoscale vortices: A new mechanism, *J. Geophys. Res.*, **93**, 6685–6693.
- Eady, E. T. (1949), Long waves and cyclone waves, *Tellus*, **1**, 33–52.
- Eckart, C. (1969), *Hydrodynamics of Oceans and Atmospheres*, 290 pp., Pergamon, Oxford, U. K.
- Frankignoul, C., and P. Muller (1979), Quasi-geostrophic response of an infinite  $\beta$ -plane ocean to stochastic forcing by the atmosphere, *J. Phys. Oceanogr.*, **9**, 104–127.
- Galperin, B., L. H. Kantha, S. Hassid, and A. Rossati (1988), A quasi-equilibrium turbulent energy model for geophysical flows, *J. Atmos. Sci.*, **45**, 55–62.
- Gill, A. E. (1982), *Atmosphere-Ocean Dynamics*, Int. Geophys. Ser., vol. 30, 662 pp., Academic, New York.
- Gill, A. E., J. S. A. Green, and A. J. Simmons (1974), Energy partition in the large-scale ocean circulation and the production of mid-ocean eddies, *Deep Sea Res.*, **21**, 499–528.
- Griffiths, R. W., and E. J. Hopfinger (1984), The structure of mesoscale turbulence and horizontal spreading of ocean fronts, *Deep Sea Res.*, **31**, 245–269.
- Holt, J. T., and I. D. James (2001), An  $s$  coordinate density evolving model of the northwest European continental shelf 1, Model description and density structure, *J. Geophys. Res.*, **106**(C7), 14,015–14,034.
- Holt, J., and R. Proctor (2008), The seasonal circulation and volume transport on the northwest European continental shelf: A fine-resolution model study, *J. Geophys. Res.*, **113**, C06021, doi:10.1029/2006JC004034.
- Holt, J. T., and L. Umlauf (2008), Modelling the tidal mixing fronts and seasonal stratification of the northwest European continental shelf, *Cont. Shelf Res.*, **28**, 887–903.
- Hoskins, B. J. (1975), The geostrophic momentum approximation and the semi-geostrophic equations, *J. Atmos. Sci.*, **32**, 233–242.
- James, I. D. (1996), Advection schemes for shelf sea models, *J. Mar. Syst.*, **8**, 237–254.
- Killworth, P. D., N. Paldor, and M. E. Stern (1984), Wave propagation and growth on a surface front in a two-layer geostrophic current, *J. Mar. Res.*, **42**, 761–785.
- Kostianoy, A. G., and I. M. Belkin (1989), A survey of observations on intrathermocline eddies in the world ocean, in *Mesoscale/Synoptic Coherent Structures in Geophysical Turbulence*, edited by J. C. J. Nihoul and B. M. Jamart, pp. 821–841, Elsevier, Amsterdam.
- Linden, P. F., B. M. Boubnov, and S. B. Dalziel (1995), Source-sink turbulence in a rotating stratified fluid, *J. Fluid Mech.*, **298**, 81–112.
- Lindzen, R. S., and B. Farrell (1980), A simple approximate result for the maximum growth rate of baroclinic instabilities, *J. Atmos. Sci.*, **37**, 1648–1654.
- Lorenz, E. N. (1955), Available potential energy and the maintenance of the general circulation, *Tellus*, **7**, 157–167.
- McWilliams, J. C. (1985), Submesoscale, coherent vortices in the ocean, *Rev. Geophys.*, **23**, 165–182.
- Mellor, G. L., and T. Yamada (1974), A hierarchy of turbulence closure models for planetary boundary layers, *J. Atmos. Sci.*, **31**, 1791–1806.
- Okubo, A. (1970), Horizontal dispersion of floatable particles in the vicinity of velocity singularity such as convergences, *Deep Sea Res.*, **17**, 445–454.
- Orlansky, I. (1969), The influence of bottom topography on the stability of jets in a baroclinic fluid, *J. Atmos. Sci.*, **26**, 1216–1969.
- Pedlosky, J. (1964), The stability of currents in the atmosphere and the ocean: Part I, *J. Atmos. Sci.*, **21**, 201–219.
- Pingree, R. D. (1978), Cyclonic eddies and cross-frontal mixing, *J. Mar. Biol. Assoc. U. K.*, **58**, 955–963.
- Pingree, R. D. (1979), Baroclinic eddies bordering the Celtic Sea in late summer, *J. Mar. Biol. Assoc. U. K.*, **59**, 689–698.
- Shapiro, G. I., and S. L. Meschanov (1991), Distribution and spreading of Red Sea Water and salt lens formation in the northwest Indian Ocean, *Deep Sea Res.*, **38**, 21–34.
- Sharples, J., and J. H. Simpson (1993), Periodic frontogenesis in regions of freshwater influence, *Estuaries*, **16**, 74–82.
- Sharples, J., C. M. Moore, T. P. Rippeth, P. M. Holligan, D. J. Hydes, N. R. Fisher, and J. H. Simpson (2001), Phytoplankton distribution and survival in the thermocline, *Limnol. Oceanogr.*, **46**, 486–496.
- Simpson, J. H., and J. R. Hunter (1974), Fronts in the Irish Sea, *Nature*, **250**, 404–406.
- Simpson, J. H., and I. D. James (1986), Coastal and estuarine fronts, in *Baroclinic Processes on Continental Shelves, Coastal and Estuarine Shelf Sci.*, vol. 3, edited by N. Mooers, pp. 63–93, AGU, Washington, D. C.
- Smagorinsky, J. (1963), General circulation experiments with the primitive equations, *Mon. Weather Rev.*, **91**, 99–164.
- Smith, K. S. (2007), The geography of linear baroclinic instability in Earth’s oceans, *J. Mar. Res.*, **65**, 655–683.
- Smith, S., and E. G. Banke (1975), Variation of the sea surface drag coefficient with wind speed, *Q. J. R. Meteorol. Soc.*, **101**, 665–673.
- Song, Y., and D. Haidvogel (1994), A semi-implicit ocean circulation model using a generalized topography-following coordinate system, *J. Comput. Phys.*, **115**, 228–244.
- Spall, M. (2000), Generation of strong mesoscale eddies by weak ocean gyres, *J. Mar. Res.*, **58**, 97–116.
- Stegner, A., and D. G. Dritschel (2000), A numerical investigation of the stability of isolated shallow water vortices, *J. Phys. Oceanogr.*, **30**, 2562–2573.
- Strass, V. H., H. Leach, and J. D. Woods (1992), On the seasonal development of mesoscale variability: The influence of the seasonal pycnocline formation, *Deep Sea Res.*, **39**, 1627–1639.

- Thiem, O., J. Berntsen, and B. Gjevik (2006), Development of eddies in an idealised shelf slope area due to an along slope barotropic jet, *Cont. Shelf Res.*, **26**, 1481–1495.
- Thomas, H., Y. Bozec, K. Elkalay, and H. J. W. de Baar (2004), Enhanced open ocean storage of CO<sub>2</sub> from shelf sea pumping, *Science*, **304**, 1005–1008.
- Thomas, L. N. (2008), Formation of intrathermocline eddies at ocean fronts by wind-driven destruction of potential vorticity, *Dyn. Atmos. Oceans*, **45**, 252–273.
- van Aken, H. M., G. J. F. van Heijst, and L. R. M. Maas (1987), Observations of fronts in the North Sea, *J. Mar. Res.*, **45**, 579–600.
- Waugh, D. W., E. R. Abraham, and M. M. Bowen (2006), Spatial variations of stirring in the surface ocean: A case study of Tasman Sea, *J. Phys. Oceanogr.*, **36**, 526–542.
- Weiss, J. (1991), The dynamics of enstrophy transfer in two-dimensional hydrodynamics, *Physica D*, **48**, 273–294.
- Williams, R. G., and M. J. Follows (2003), Physical transport of nutrients and the maintenance of biological production, in *Ocean Biogeochemistry: The Role of the Ocean Carbon Cycle in Global Change*, edited by M. Fasham, pp. 19–51, Springer, New York.
- Williams, R. G., C. Wilson, and C. W. Hughes (2007), Ocean and atmosphere storm tracks: The role of eddy vorticity forcing, *J. Phys. Oceanogr.*, **37**, 2267–2289.
- Wunsch, C. (1998), The work done by the wind on the ocean general circulation, *J. Phys. Oceanogr.*, **28**, 2332–2340.
- Yanagi, T., T. Shimizu, and T. Matsuno (1996), Baroclinic eddies south of Cheju Island in the East China Sea, *J. Oceanogr.*, **52**, 763–769.
- Zatsepin, A. G., A. I. Ginzburg, A. G. Kostianoy, V. V. Kremenetskiy, V. G. Krivosheya, S. V. Stanichny, and P.-M. Poulain (2003), Observations of Black Sea mesoscale eddies and associated horizontal mixing, *J. Geophys. Res.*, **108**(C8), 3246, doi:10.1029/2002JC001390.
- Zhurbas, V., T. Stipa, P. Mälkki, V. Paka, N. Golenko, I. Hense, and V. Sklyarov (2004), Generation of subsurface cyclonic eddies in the southeast Baltic Sea: Observations and numerical experiments, *J. Geophys. Res.*, **109**, C05033, doi:10.1029/2003JC002074.

G. Badin and R. G. Williams, Department of Earth and Ocean Sciences, University of Liverpool, Liverpool L69 3GP, UK. (gualti@liverpool.ac.uk)

L. J. Fernand, Centre for Environment, Fisheries and Aquaculture Science, Lowestoft NR33 0HT, UK.

J. T. Holt, Proudman Oceanographic Laboratories, Joseph Proudman Building, 6 Brownlow Street, Liverpool L3 5DA, UK.